The multiple activations in budding yeast S-phase checkpoint are Poisson processes

Xin Gao [ID][a], Peijie Zhou[b] and Fangting Li [ID][a,*]

[a]School of Physics, Center for Quantitative Biology, Peking University, Beijing 100871, China
[b]Department of Mathematics, University of California, Irvine, CA 92697, USA
*To whom correspondence should be addressed: Email: lft@pku.edu.cn
Edited By: Li-Jun Ma

Abstract

Eukaryotic cells activate the S-phase checkpoint signal transduction pathway in response to DNA replication stress. Affected by the noise in biochemical reactions, such activation process demonstrates cell-to-cell variability. Here, through the analysis of microfluidics-integrated time-lapse imaging, we found multiple S-phase checkpoint activations in a certain budding yeast cell cycle. Yeast cells not only varied in their activation moments but also differed in the number of activations within the cell cycle, resulting in a stochastic multiple activation process. By investigating dynamics at the single-cell level, we showed that stochastic waiting times between consecutive activations are exponentially distributed and independent from each other. Finite DNA replication time provides a robust upper time limit to the duration of multiple activations. The mathematical model, together with further experimental evidence from the mutant strain, revealed that the number of activations under different levels of replication stress agreed well with Poisson distribution. Therefore, the activation events of S-phase checkpoint meet the criterion of Poisson process during DNA replication. In sum, the observed Poisson activation process may provide new insights into the complex stochastic dynamics of signal transduction pathways.

Keywords: budding yeast, S-phase checkpoint, stochasticity, Poisson activation process

---

Significance Statement

Biological noise introduces cell-to-cell variability in the signal transduction process, which may demonstrate complex dynamic characteristics. In the previous study, the S-phase checkpoint activation was modeled as a stochastic barrier-crossing process in a double-well potential landscape. Here, after investigating both the activation and recovery processes, we discovered Poisson process of multiple activations in the yeast S-phase checkpoint through single-cell experiments and statistical analysis. We quantitatively proved that the waiting time for each activation is independently and identically distributed as an exponential distribution. A simple Poisson process model parametrized by DNA replication stress intensity was proposed to describe the number of activation events, both in wild-type and mutant strains.

Introduction

Biological noise, i.e. the stochasticity of biochemical reactions, is crucial for many biological processes (1). Noisy signals through a combination of positive and negative feedback loops may affect bi-stability, oscillation, and other dynamic characteristics (2, 3). By regulating gene expression, biological noise can determine cell differentiation (4), circadian rhythms (5), and cell fate transition (6). Through observation of fluorescent reporters of gene expression at the single-cell level, we can quantitatively investigate the intensity of noise and its effects on biological processes (7).

Noise also plays multiple roles in the signal transduction pathway, such as limiting channel capacity and enhancing dynamic signal processing (8, 9). In a system with positive feedback, noisy signals can be amplified and therefore result in cell-to-cell variations, which induce different responses of individual cells to the same environmental stimulus (10, 11). Also, noisy fluctuations in oscillatory systems may facilitate signal amplification and induce various responses through stochastic resonance (12). Binary and graded responses, or their combinations, are the common activation modes in signal transduction (13, 14). These response patterns are indistinguishable under an average response level in a cell population, but they can be captured at the single-cell level (15). Thus, identifying cell-to-cell variability at the single-cell level in numerous cells, either by time-lapse fluorescence microscopy or by single-molecule RNA fluorescence in situ hybridization (smRNA FISH) (16), forms the basis for investigating the dynamic activation of signal transduction pathways.

In response to the DNA replication stress signal, the S-phase checkpoint signal transduction pathway activates to facilitate the progress of DNA replication and maintain genomic integrity (17). In the presence of the positive feedback loop, the activation moment of the S-phase checkpoint in budding yeast demonstrates cell-to-cell variability under DNA replication stress triggered by stochastic noise (18). The positive feedback loop in the S-phase checkpoint arising from Rad53 phosphorylation can be modeled as a double-well potential, where biochemical reactions facilitate a barrier-crossing process for the activation (19). Meanwhile, the recovery process of the S-phase checkpoint, which incorporates a negative feedback loop, relieves DNA replication stress (20). We remain unclear on how the recovery process of the S-phase checkpoint influences the overall dynamic properties of the S-phase checkpoint system (21). Generally, a network with both positive and negative feedback loops may exhibit oscillatory behaviors, e.g. the p53 and NF-κB signal transduction pathways (22, 23). However, with strong biological noise, the S-phase checkpoint may demonstrate more complex dynamic characteristics.

Herein, through microfluidics-integrated time-lapse imaging in live cells and deep learning-based image analysis methods, we analyzed the dynamics of S-phase checkpoint activation and inactivation in *Saccharomyces cerevisiae* at the single-cell level. Under different levels of DNA replication stress induced by hydroxyurea (HU), we found that S-phase checkpoint in budding yeast can be activated stochastically multiple times within a single-cell cycle. The waiting times of each activation are independently and identically distributed, suggesting that activation of the S-phase checkpoint pathway is a Poisson process, the duration of which is determined by DNA replication time. Indeed, the number of activation events in a cell cycle follows a Poisson distribution. A simple Poisson process model parametrized by HU can well describe the number of activation events in both wild-type (WT) and mutant strains. Overall, the dynamics of the observed Poisson activation process are distinct from other well-studied signaling transduction pathways.

Results

Activation and inactivation processes of S-phase checkpoint in budding yeast

We first provide an overview of the regulatory network engaged in S-phase checkpoint activation and inactivation of budding yeast. The activation of S-phase checkpoint is initialized by several types of events that perturb replication fork progression, such as nucleotide deficiency, DNA damage and DNA secondary structure (24). Hydroxyurea (HU) is experimentally used to induce DNA replication stress and trigger the activation of the S-phase checkpoint by inhibiting the activity of ribonucleotide reductase (RNR) (25). RNR catalyzes a redox reaction to produce natural deoxynucleoside diphosphates (dNDPs) required for their subsequent de novo synthesis (26), but the inactivation of RNR induces a reduction of the dNTP pool and the accumulation of single-stranded DNA (ssDNA) in S-phase (27). Induced by the accumulation of ssDNA, DNA replication stress then provides the upstream signal for Rad53 phosphorylation mediated by sensor Mec1 and adaptors Rad9 and Mrc1 (28, 29). Consequently, phosphorylated Rad53 (Rad53p) amplifies upstream signals through autophosphorylation, forming a positive feedback loop. Also, Rad53p phosphorylates Dbf4 to decrease the concentration of DDK, an essential kinase for DNA replication, thus preventing further accumulation of ssDNA (30, 31), resulting in the formation of a negative feedback loop. Meanwhile, by phosphorylating kinase Dun1 (21), Rad53p promotes the transcription of *RNR2/3/4* to increase the dNTP pool for DNA synthesis (32), thus forming another negative feedback. As a result, the reduction of ssDNA eventually alleviates the upstream DNA replication stress signal which, in turn, results in the inactivation of S-phase checkpoint in a recovery process (20), during which the Rad53p tends to return to its normal level. However, when exposed to a persistent DNA damage signal, S-phase checkpoint may be activated again by the excess of ssDNA at the new location of stalled replication fork to then repeat the cyclic dynamics, resulting in multiple activations of the checkpoint within one cell cycle. Overall, the combination of both positive and negative feedback loops plays an important role during the activation and inactivation processes of S-phase checkpoint. In addition, the prevalence of stochastic noise in signaling pathways within budding yeast may further induce even more complex activation patterns at the single-cell level.

To investigate the dynamics of S-phase checkpoint, we simplified the above processes into a network shown in Fig. 1A, including the key kinase Rad53, ssDNA, and RNR (18). For convenience, we use "activation" to denote the activation of S-phase checkpoint below.

S-phase checkpoint is activated multiple times during a cell cycle

The phosphorylation of kinase Rad53 plays an essential role in the activation of S-phase checkpoint. Consequently, measuring the level of Rad53p in a single yeast cell is crucial for determining the state of S-phase checkpoint. We have developed a method to temporally quantify Rad53p level in single cells by the level of Rnr3, the transcription of which is regulated by Rad53p (19). To accomplish this, we fused Rnr3 with GFP and quantified Rnr3 levels at the single-cell level by microfluidics-integrated time-lapse fluorescence imaging. Meanwhile, with a customized cell segmentation and tracking algorithm, we extracted the temporal fluorescence intensity variation of each cell from the images for hundreds of cells (see Materials and Methods section).

For each HU concentration, we collected temporal fluorescence data for around 300 cells at a 5-min time resolution for 8 h of the WT strain (see Materials and Methods section). Through the time-window fitting approach, we used a 15-min time-window to calculate the fluorescence growth rate (FGR) of each cell to quantify the Rad53p level and thus determine the state of S-phase checkpoint (see Materials and Methods section, Online Supplementary Fig. S1). We found that cell-to-cell variability not only lies in the moment of activations but also in the number of activations in a cell cycle, which is denoted as X, leading to the multiple activations of S-phase checkpoint. We demonstrated the temporal variations of Rnr3 and FGR in different cells that activated once and twice under 100 mM HU stimulation in Fig. 1B. Among them, cells activated once ($X = 1$) exhibit a heterogeneous increase in Rnr3 level and a pulse in FGR level, whereas inactivated cells without the activation of the S-phase checkpoint exhibit no obvious increase in Rnr3 level. For cells activated twice ($X = 2$), the Rnr3 level rises during the first activation and reaches a stable value and then rises again during the second activation, causing two heterogeneous pulses in FGR. For comparison, in the absence of HU stimulation, cells are not activated in a cell cycle; instead, they exhibit stable and low Rnr3 and FGR levels over time (Online Supplementary Fig. S3). Under low concentration HU stimulation, the phenomenon of multiple activations is hard to be observed (20-, 30-, and 40-mM HU, Online Supplementary Fig. S1).

To quantitatively study the activation and inactivation process of S-phase checkpoint, we have developed maximum
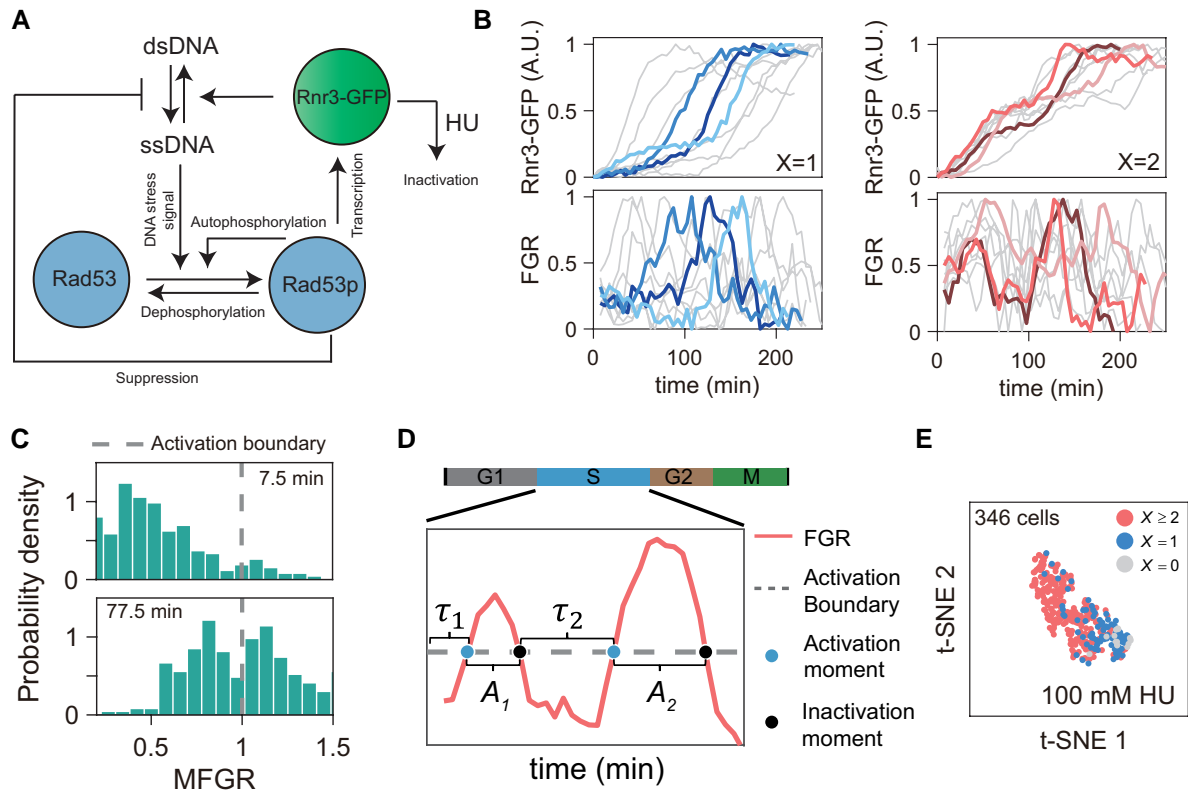
Fig. 1. Multiple activations in budding yeast S-phase checkpoint. A) Schematic diagram of the S-phase checkpoint pathway. HU inhibits the activity of RNR and then suppresses the synthesis of dsDNA. DNA replication stress signal promotes the phosphorylation of Rad53 and the autophosphorylation of Rad53p, forming positive feedback. Rad53p prevents DNA deconvolution through a downstream pathway and mediates the transcription of RNR to repair upstream DNA damage, forming negative feedback loops. B) Left panel: Rnr3 fluorescence and FGR of 10 cells that activated once ($X = 1$), where three cells among them are highlighted. Rnr3 and FGR share the same x-axis. Rnr3 fluorescence and FGR of each cell were normalized between 0 and 1. Right panel: Rnr3 fluorescence and FGR of 10 cells that activated twice ($X = 2$), where three cells are highlighted. C) Under 100 mM HU stimulation, MFGR distribution shows a single modal at 7.5 min, whereas it shows a bimodal distribution at 77.5 min (see Online Supplementary Fig. S4). Dotted lines denote the activation boundary. D) The activation boundary defines the waiting time (τ_i) and activation duration (A_i) for the ith activation of a single cell. Activation and inactivation moments are marked by dots. E) Rnr3 fluorescence data after dimensionality reduction by t-SNE with 100 mM HU. Cells are labeled by the number of activations X into three groups ($X = 0$, $X = 1$, and $X \geq 2$).

fluorescence growth rate (MFGR), which is defined as the maximum value of FGR during time $[0, t]$, i.e. $\mathrm{MFGR}(t) \triangleq \max_{0 \leqslant s \leqslant t} \mathrm{FGR}(s)$, to determine whether the cell has activated up to moment t (see Materials and Methods section) (19). Under HU stimulation, the activation of the S-phase checkpoint demonstrates a binary response in a cell population, resulting in the bimodal distribution of MFGR (Fig. 1C and Online Supplementary Fig. S4). During the activation process, the FGR of a single cell increases and does so across the activation boundary between the peaks of MFGR bimodality, showing that the cell switches from inactive to active state. Thus, when the FGR of a cell is above the activation boundary, the cell is considered to be in the activated state; otherwise, it is in the inactivated state. Accordingly, we can calculate the proportion of cells that have not been activated from time 0 to t ($R_{in}(t)$). Moreover, by comparing the FGR curve of each cell with the activation boundary, we can obtain the activation duration of the possible ith activation A_i, the waiting time for the possible ith activation τ_i, and the number of activations X of the cell (Fig. 1D).

The rationale for determining the number of activations X of a cell by the FGR-based method can be supported by adopting the t-distributed stochastic neighbor embedding (t-SNE) dimensionality reduction method (33) on the raw Rnr3 fluorescence data. In the reduced 2D space, we labeled the cells using the X number generated by the FGR-based method and discovered that cells with the same X number are clustered under 100 mM HU stimulation (Fig. 1E). Therefore, the aggregation of cells with the same X in the 2D t-SNE space indicates that cells with the same X share close characteristics.

Waiting times between sequential activations are independently and identically distributed

To investigate the relationship between the first and second activation in single cells, we set the moment of entry into S-phase to 0 for each cell and calculated the proportion of cells that have not been activated $R_{in}(t)$ over time. In Fig. 2A, we derived the logarithm of $R_{in}(t)$, notated as the inactivation curve, and found that the inactivation curve decays linearly over time, which satisfies $ln(R_{in}(t)) = -\lambda_1 t$, where λ_1 represents the activation rate of the first activation ($\lambda_1 = 0.0133$). Since length of the cell cycle is finite, we introduced a normalization factor a to normalize the probability density of the waiting time for the first activation from 0 to its maximal value among activated cells and found that the curve $P(\tau_1) = a_1 \lambda_1 e^{-\lambda_1 \tau_1}$ can fit the distribution of waiting time for first activation τ_1 (Fig. 2A). These results suggest that the waiting time for first activation is exponentially distributed.

Similarly, we studied the dynamics of the second activation process by setting the end moment of the first activation as moment 0 for each $X \geq 1$ cell. We mapped the inactivation curve of
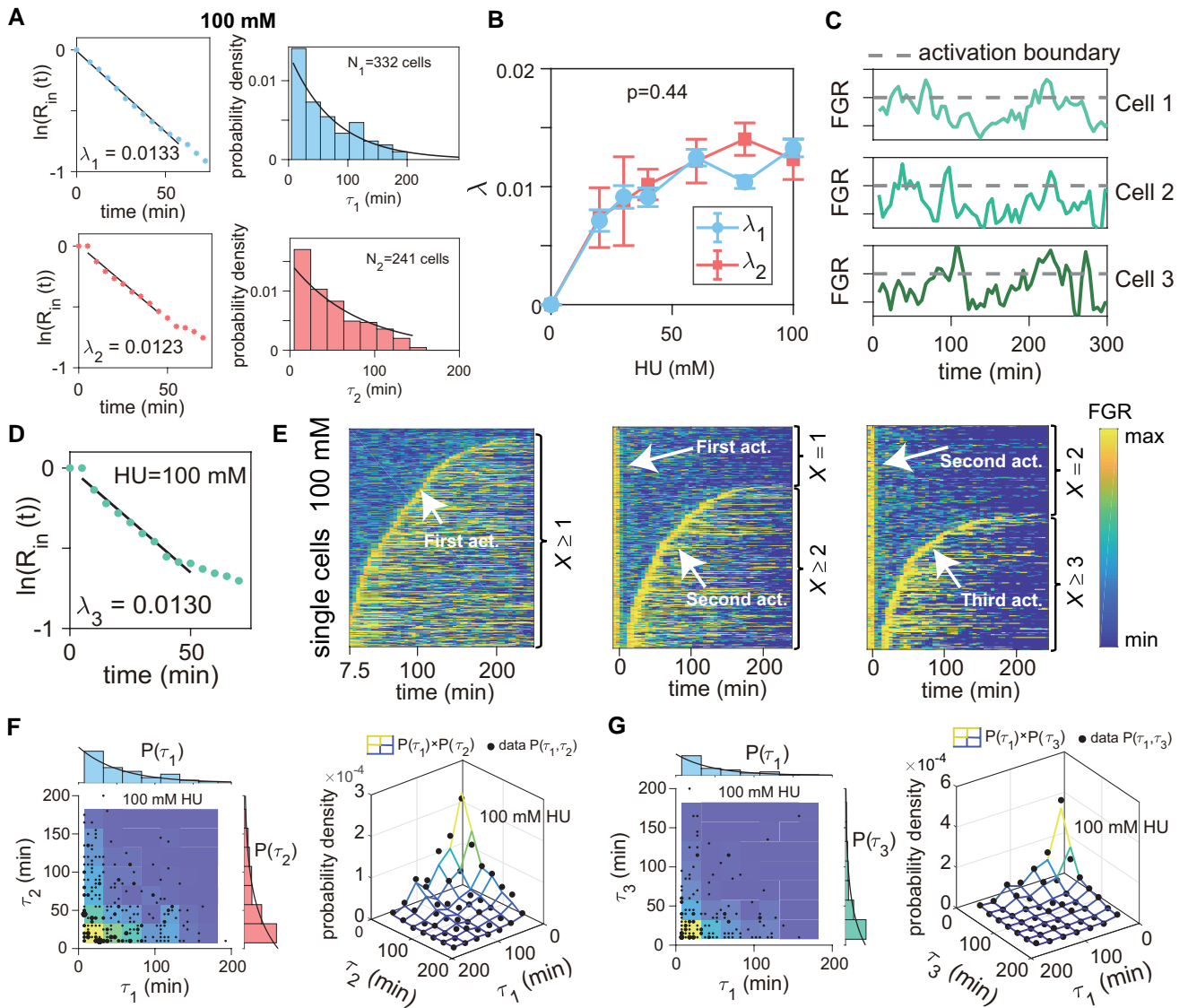
Fig. 2. Waiting times between sequential activations are identically and independently distributed. A) Left panel: Inactivation curve of the first (upper) and the second (bottom) activations under 100 mM HU, where the y label denotes the logarithm of the percentage of inactive cells. Moment 0 of the first inactivation curve indicates the moment of each cell entering S-phase, whereas moment 0 of the second inactivation curve denotes the inactivation moment of the first activation for each cell. λ of each activation was obtained by fitting the slope of the linear region of corresponding inactivation curve. Right panels denote the distribution of τ_1 (N = 332 cells) and τ_2 (N = 241 cells), where the solid line shows curve $a\lambda e^{-\lambda t}$, where a is the normalization factor. B) First (λ_1) and the second (λ_2) activation rate under various HU concentrations (0, 20, 30, 40, 60, 80, and 100 mM), paired-test, $P = 0.44$. Error bar denotes the SD of fitting the inactivation curves. C) FGR of three cells that activated three times in a cell cycle. Dotted lines denote the activation boundary. D) Inactivation curve of the third activations under 100 mM HU, where moment 0 denotes the inactivation moment of the second activation for each cell. E) Left panel: Heatmaps of temporal FGR variations in single cells with 100 (N = 346 cells) mM HU, where cells are sorted by the waiting time of first activations τ_1. Color denotes the value of FGR, and we set the FGR of each cell beyond its cell cycle to 0. Middle panel: Setting the inactivation moment of the first activation for each cell as moment 0, we plotted the heatmaps of temporal FGR variations, where cells were sorted by τ_2. Right panel: Setting the inactivation moment of the second activation for each cell as moment 0, we plotted the heatmaps of temporal FGR variations in single cells, where cells were sorted by τ_3. F) Left panel: Joint distribution of τ_1 and τ_2 of $X \geq 2$ cells under 100 mM HU. Each dot denotes a single cell, and the color denotes the probability density of joint distribution ($P(\tau_1, \tau_2)$). Bar above denotes the distribution of τ_1 ($P(\tau_1)$), whereas the bar on the right side denotes the distribution of τ_2 ($P(\tau_2)$). Right panel: Comparison of probability densities of $P(\tau_1) \times P(\tau_2)$ (grid lines) and $P(\tau_1, \tau_2)$ (dots). G) Left panel shows the joint distribution of τ_1 and τ_3 of cells activated three times under 100 mM HU. Right panel shows the comparison of $P(\tau_1) \times P(\tau_3)$ and $P(\tau_1, \tau_3)$. Details were the same in panel (F).

the waiting time for second activation τ_2 and found that τ_2 of $X = 2$ cells is also exponentially distributed (Fig. 2A). The calculated activation rate of the second activation ($\lambda_2 = 0.0123$) is close to that of the first activation with 100 mM HU. By changing HU concentration, we found that the waiting time of both the first and second activation events also follows exponential distribution (Fig. 2B and Online Supplementary Fig. S5). The activation rate was positively correlated with different HU concentrations, approaching

saturation at around 60 mM HU, and no significant difference was observed between λ_1 and λ_2 (paired t-test, P-value=0.44). The conclusion that the values of λ_1 and λ_2 are close is robust and independent of the choice of activation boundaries (Online Supplementary Fig. S7). Overall, with the same HU concentration, the waiting times for possible first and second activations follow an identical exponential distribution. To further verify that the multiple activations are identically distributed, we investigated

the possible third activation. Under the stimulation of 100 mM HU, we found that the FGR of still another part of the cells would have three peaks, indicating that these cells had been activated three times in a cell cycle (Fig. 2C). Setting the end moment of the second activation to 0, we also found no significant difference between λ_3 and the first two activation rates under 100 mM HU stimulation (Fig. 2D).

We ranked the cells by τ_1 and mapped the heatmaps of temporal FGR variations with 100 mM HU. Figure 2E intuitively demonstrates cell-to-cell variability in waiting time for the first activation among a cell population, for which the activation moment shows a nonlinear distribution (Fig. 2E). When the range of y-axis is [0, 1], the first activation curve in the heatmap satisfied $(1 - e^{-\lambda_1 t})$. Setting the inactivation moment of the first activation as moment 0 and ranking the cells by τ_2, we can also visualize the second activation from the heatmaps of temporal FGR variations, indicating a pattern similar to that of the first activation. With the same processing, we can also see the third activation. Notably, S-phase lengths of different cells are not uniform, and some cells enter the next cycle shortly after the second activation. Thus, the second activation curve only satisfies $(1 - e^{-\lambda_2 t})$ in the early 60 min. We will discuss the time limit of activations in the next section. As shown in the heatmaps, the FGR value of activated cells is significantly higher than that of inactivated cells among a given cell population, which supports distinguishing cell states by the activation boundary threshold.

Under 100 mM HU stimulation, we selected cells with $X \geq 2$ to map the 2D distribution of τ_1 and τ_2 to test whether the first and the second activation are independent (Fig. 2F, Online Supplementary Fig. S6). We denoted the distribution of τ_1 as $P(\tau_1)$, the distribution of τ_2 as $P(\tau_2)$, and the joint distribution of τ_1 and τ_2 as $P(\tau_1, \tau_2)$ in the τ_1–τ_2 plane. The joint distribution $P(\tau_1, \tau_2)$ of $X \geq 2$ cells is almost everywhere equal to $P(\tau_1) \times P(\tau_2)$, i.e. $P(\tau_1) \times P(\tau_2) = P(\tau_1, \tau_2)$. This result is consistent with the mathematical definition of the independence of the two variables, suggesting that first and the second activation are independent for $X \geq 2$ cells. Similarly, the joint distribution of τ_1 and τ_3, $P(\tau_1, \tau_3)$, is equal to $P(\tau_1) \times P(\tau_3)$ and the first activation (Fig. 2G), suggesting that the first and third activations are also independent. We then validated the independence of the multiple activations by analyzing their inactivation curves (see Materials and Methods section, Online Supplementary Fig. S9). Overall, the multiple activations of S-phase checkpoint are independently and identically distributed, i.e. a Poisson process, and we term this multiple activation process as a Poisson activation process.

The duration of DNA replication determines the upper time limit of multiple activations

We next investigated the relationship between the Poisson activation process of the S-phase checkpoint and DNA replication. Using 100 mM HU, for the cells with $X \geq 1$, we found the smaller τ_1 to be associated with the larger proportion of cells that activate again in a cell cycle, showing a strong negative correlation (Fig. 3A, Pearson coefficient $r = -0.96$). Similarly, for cells with $X \geq 2$, the smaller $\tau_1 + \tau_2$ is, the larger the proportion of cells that could activate for a third time (Fig. 3B $r = -0.97$, Online Supplementary Fig. S6). Since S-phase checkpoint is solely activated during the S-phase (DNA replication phase), longer τ_1 represents more DNA that has completed replication. The negative correlation between τ_1 and the proportion of cells reactivated during the cell cycle implies that the probability of S-phase checkpoint activation may depend on the length of unreplicated DNA in the S-phase.

Within the S-phase of a yeast cell cycle, during waiting time τ_1 before the first activation, DNA replication will continue until either pathway activation or the end of the S-phase. Therefore, the larger value of τ_1 indicates a shorter length of unreplicated DNA. When the S-phase checkpoint is activated, the progress of DNA replication is prevented (30, 31). After completion of the checkpoint recovery process, DNA replication continues to progress until a potential second activation is triggered or until all DNA replication is completed. The second activation is induced by DNA stress signals at the different replication stage with the first activation. Therefore, we suggested that multiple activations are caused by independent DNA stress signals among different DNA replication progressions. As the DNA replication process advances, the likelihood of the pathway being activated during this DNA replication period decreases progressively. That is, the finite time for DNA replication (T) establishes an upper time limit for all potential activations, and all subsequent activations following the first activation can be viewed as a Poisson process within the remaining DNA replication time. This elucidates the negative correlation between the ratio of reactivated cells and τ_1.

To quantitatively assess the upper time limit for the Poisson activation process arising from DNA replication time, we conducted a mapping of waiting times for each activation in individual cells. Remarkably, the sum of τ_1 and τ_2 has a distinct upper limit in the $X \geq 2$ cell population (Fig. 3C). Similarly, for cells in the $X \geq 3$ population, an upper limit is set for $\tau_1 + \tau_2 + \tau_3$ (Fig. 3C). Comparing the upper limit of τ among cells with different activation numbers ($X = 1, 2,$ and 3), we observed that the upper confidence limit (UCL) of τ_1 in the $X = 1$ cell population closely matched the UCL of $\tau_1 + \tau_2$ in the $X = 2$ cell population (75% UCL, Fig. 3D). Furthermore, the UCL of $\tau_1 + \tau_2 + \tau_3$ in cells with a third activation was also similar to the upper limit of $\tau_1 + \tau_2$ with varying HU concentrations. These experimental results support that the upper limit of τ, which is independent of activation numbers, represents pure DNA replication time. Upon increasing the HU concentration, we observed a corresponding rise in the upper limit of τ and a prolongation of the cell cycle (Fig. 3D). This indicates that the DNA replication time is influenced by the HU concentration, with higher doses of HU leading to longer DNA replication times. In addition, we noticed that the duration of cell activation A remained constant across different HU concentrations, and the first activation duration A_1 closely resembled the second activation duration A_2 (Fig. 3E, Online Supplementary Fig. S10).

Therefore, our findings suggest that the DNA replication time provides a robust upper time limit for the Poisson activation process independent of the number of activations, and increasing HU concentration extends this upper time limit. At the same time, the fact that the upper time limit of the Poisson activation process, i.e. DNA replication time, is independent of the number of activations also implies that the DNA replication rate remains relatively constant during the waiting time of different activations. Combining with the identical distribution of waiting times between multiple activations (Fig. 2), it demonstrated that the intensity of upstream DNA stress signals is similar during different τ_n.

In summary, the activation process can be modeled as a Poisson process within time interval [0, T], where T is the DNA replication time and is dependent on HU concentration. Intriguingly, the rad53-S350A mutant (S350A), with impaired Rad53 autophosphorylation, also exhibits a Poisson activation process during HU stimulation, though with a lower activation rate than the WT strain (Online Supplementary Fig. S2). Notably, in other rad53 mutants, such as T354A and S350A-T354A with severely impaired Rad53 autophosphorylation, the Poisson activation process is hard to observe.
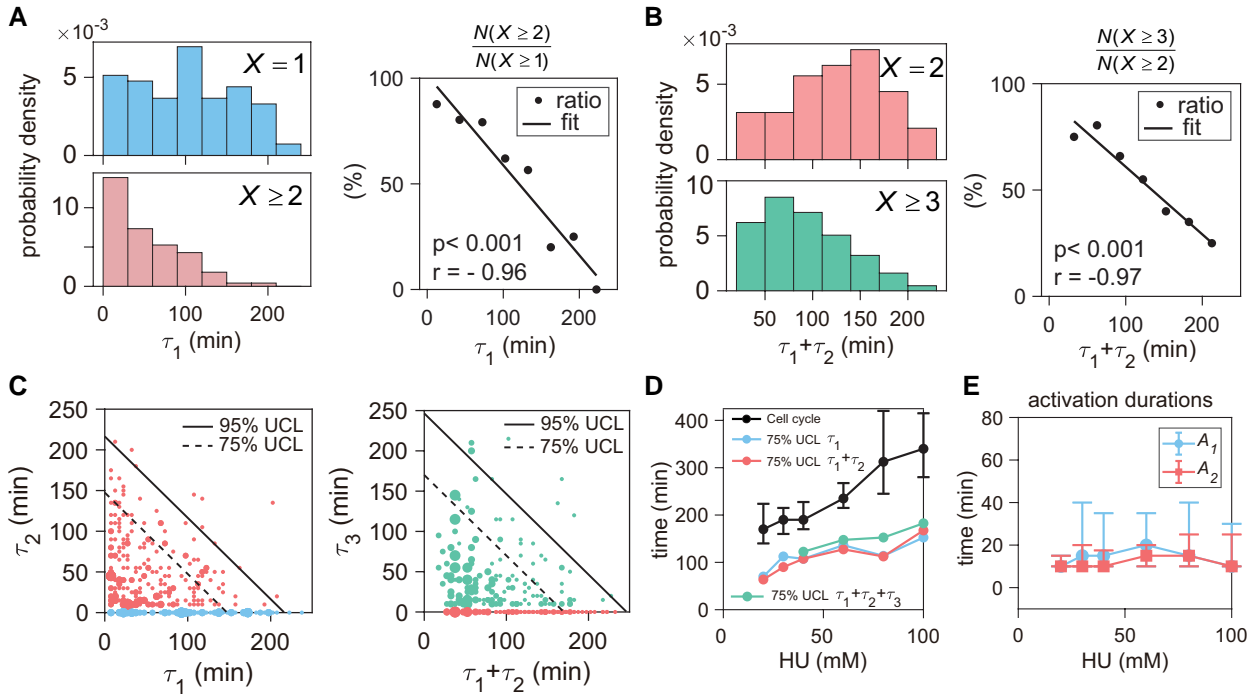
Fig. 3. Distribution of waiting times between sequential activations with 100 mM HU. A) Left panel: The τ_1 distribution of $X = 1$ cells (upper panel) and $X \geq 2$ cells (bottom panel) under 100 mM HU stimulation. Right panel: Dots represent the ratio of $X \geq 2$ cells in each τ_1 interval. The line represents a linear fit to the data points; Pearson coefficient (r) and corresponding P-value were also shown in the panel. B) Left: The $\tau_1 + \tau_2$ distribution of $X = 2$ cells (upper panel) and $X \geq 3$ cells (bottom panel) with 100 mM HU. Right: Ratio of $X \geq 3$ cells in each $\tau_1 + \tau_2$ interval. Details are the same in (A). C) Left panel: We set the τ_2 of $X = 1$ cells as 0 (blue dots), and mapped the joint distribution of τ_1 and τ_2 of all activated cells, where red dots denote the $X \geq 2$ cells. Solid line denotes the 95% upper confidence limit (UCL) of $\tau_1 + \tau_2$, where the dotted line denotes the 75% UCL. Right panel: We set the τ_3 of $X = 2$ cells as 0 (red dots), and mapped the joint distribution of $\tau_1 + \tau_2$ and τ_3 of all $X \geq 2$ cells, where green dots denote the cell population where $X \geq 3$. D) With various HU concentrations, the cell cycle, the 75% UCL of τ_1 for $X = 1$ cells, $\tau_1 + \tau_2$ for $X = 2$ cells and $\tau_1 + \tau_2 + \tau_3$ for $X = 3$ cells, as shown, respectively. Data of cell cycle are median with interquartile range (IQR). E) Durations of the first (A_1) and the second activations (A_2) with various HU concentrations. Data are median with IQR.

The event of multiple activations is a Poisson process

We have investigated the underlying biological mechanism in the Poisson activation process of S-phase checkpoint. To further validate our understanding of the S-phase checkpoint, we built a phenomenological Poisson process model to describe the probability of activation under different HU concentrations during DNA replication (Fig. 4A). We introduced two parameters in our phenomenological model, T and λ, where T is DNA replication time and λ is the activation rate. Both T and λ are dependent on HU concentration ([HU]). The number of activations $X(\lambda, T)$ follows a Poisson distribution with mean λT (see Materials and Methods section) as

$$P(X(\lambda, T) = k) = \frac{(\lambda T)^k}{k!} e^{-\lambda T}, \quad k = 0, 1, 2, \ldots. \tag{1}$$

We made two assumptions here. First, we ignored the DNA replication process during activation duration, i.e. the number of activations X does not affect the DNA replication time T, which is supported by the fact that the upper limit of τ_1 is close to the upper limit of $\tau_1 + \tau_2$. Second, we ignored the heterogeneity of the origin of replication and simply assumed that the activation rate λ is uniform and consistent during time $[0, T]$. In that case, the DNA replication stress signal is the average signal of all replication forks.

We first investigated the relationship between λ and HU concentration. Figure 2B shows that λ will increase with HU and tends

to saturate at HU greater than 60 mM. Thus, we used the Hill function to describe the relationship between λ and HU as

$$\lambda = \lambda_m \frac{[\text{HU}]^n}{[\text{HU}]^n + K_\lambda^n}. \tag{2}$$

Fitting the equation to the data, we found the best fit parameter values are $\lambda_m = 0.013 \text{min}^{-1}$, $K_\lambda = 19.5 \text{mM}$ and $n = 2$ (Fig. 4B).

Next, we studied the relationship between T and HU concentration. HU affects replication time by altering the replication rate α of DNA (25), and the replication time T can be approximated by $T = \frac{L}{\alpha N_R}$, where $L = 1.3 \times 10^7$ bp is the length of DNA, and $N_R = 600$ is the number of replication origins (2, 34). We used the Hill function to describe how HU concentration influences the replication rate α as $\alpha = \alpha_0 \frac{K_\alpha^m}{K_\alpha^m + [\text{HU}]^m}$, where m and K_α are constants. α_0 denotes the replication rate without HU, which equals $1.6 \pm 0.3 \text{kb/min}$ (34). We also examined the power-law model to calculate the replication rate α in Online Supplementary Fig. S11. Then, we fit the relationship between X and HU concentration by Eq. 1, with the best fit parameters of the Hill model, $K_\alpha = 0.89 \text{mM}$ and $m = 0.53$ (see Table 1). We found that our models could well describe the probability of number of activations X during a cell cycle and that the measured number of activations follows the Poisson distribution calculated by Eq. 1 under different HU concentrations (Fig. 4C). DNA replication time estimated by our model is close to the 75% UCL of $\tau_1 + \tau_2$ (Fig. 4D). We could also verify whether it is a Poisson process by comparing the expectation and variance of X. Since an event more than three times X is difficult to identify
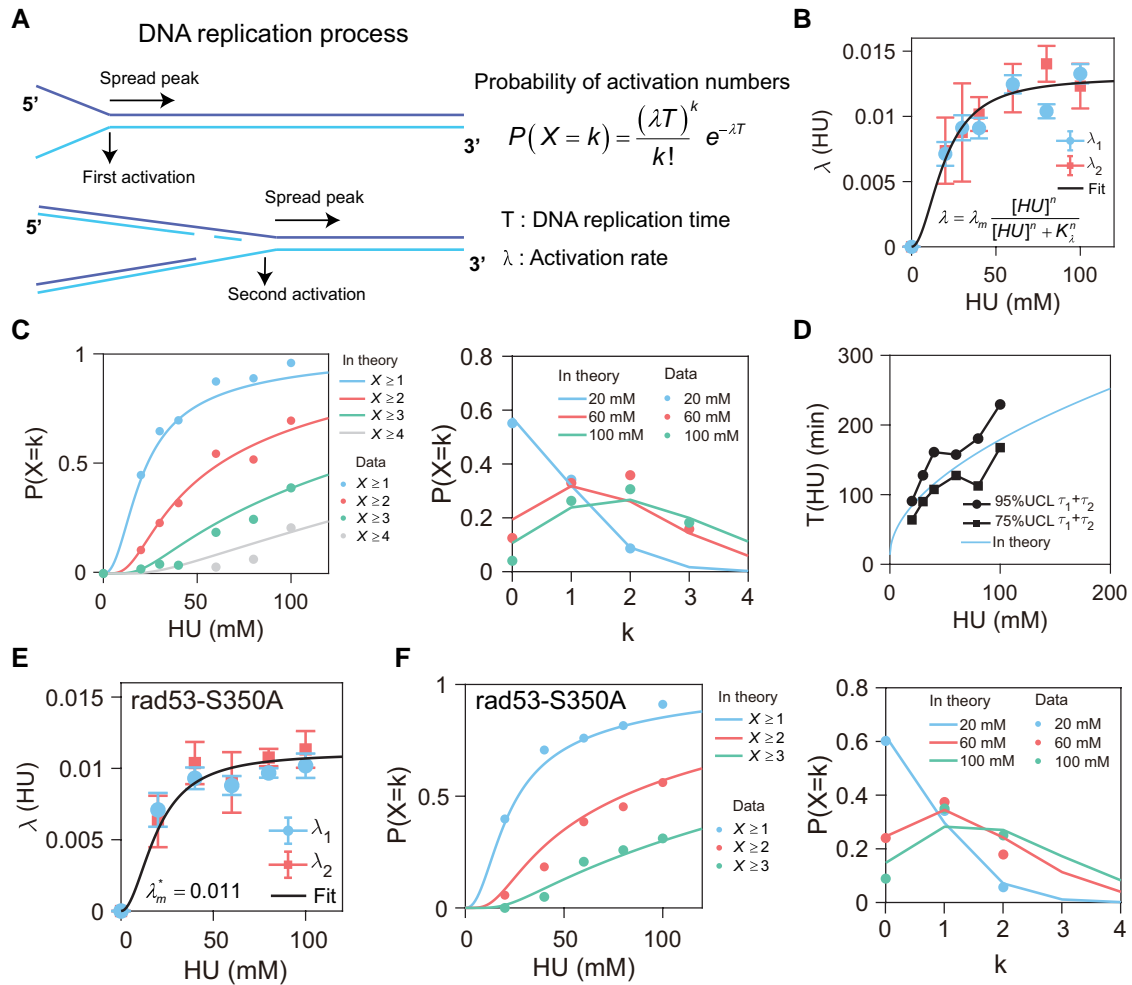
Fig. 4. The event of multiple activations is a Poisson process. A) Schematic diagram of the first and the second activation during DNA replication progression. The spread peaks were at different DNA replication progressions during the first the second activations. B) Fitting the λ_1 and λ_2 activation rate at the same time by Eq. 2 in WT strain. The best fit parameters are $\lambda_m = 0.013\text{min}^{-1}$, $K_\lambda = 19.5\text{mM}$, and $n = 2$. C) Left panel: Using the Hill model to describe the relationship between T and $[HU]$, our model can fit the probability of number of activations in a cell cycle among a cell population under different HU concentrations. The lines denote the probability of $X \geq 1$, $X \geq 2$, $X \geq 3$, and $X \geq 4$ cells in a population calculated by our model, where the dots denote the measured probability of $X \geq 1$, 2, 3 and 4 cells in a population. Right panel: Comparison of measured (dots) and calculated (lines) probability of $X = 0$, 1, 2, and 3 among a cell population under 20, 60, and 100 mM HU, respectively. D) Comparison of the 75 and 95% UCL of $\tau_1 + \tau_2$ to the replication time T predicted by our model. E) Fitting the λ_1 and λ_2 activation rate by Eq. 2 at the same time in *rad53-S350A* mutant. The best fit parameters are $\lambda_m^* = 0.011\text{min}^{-1}$, $K_\lambda = 19.5\text{mM}$, and $n = 2$. F) In the *rad53-S350A* mutant, our model well describes the probability of $X \geq 1$, 2, and 3 cells among a population under various HU concentrations, respectively. Details are the same in panel (C).

Table 1. The descriptions, values, and sources of parameters in our model.

Parameters	Descriptions	Values (mean with SD)	Sources
L	DNA length	1.3×10^4 kb	(2)
α_0	Replication rate of each fork	1.6 ($\pm$0.3) kb/min	(34)
N_R	Number of active replication forks	~600	(34)
λ_m	Maximal activation rate of WT	0.013 ($\pm$0.0065) min^{-1}	Fit
λ_m^*	Maximal activation rate (S350A)	0.011 ($\pm$0.0056) min^{-1}	Fit
K_λ	Hill coefficient of activation rate	19.5 ($\pm$9.7) mM	Fit
m	Order of replication for Hill model	0.53 ($\pm$0.019)	Fit
K_α	Hill coefficient of replication rate	0.89 ($\pm$0.17) mM	Fit

precisely, we herein compared the theoretical and experimental expectations and variances at $X = 0$, 1, and 2 (Online Supplementary Fig. S11). The theoretical predictions of the expectations and variances are close to the measured values under different HU concentrations. These facts support that the event of multiple activations is a Poisson process during DNA replication time.

We further validated our phenomenological model by introducing the rad53 autophosphorylation site mutant *rad53-S350A*, which only influences the autophosphorylation of Rad53 and does not affect the replication time in theory. We measured the activation rate of S350A mutant by fitting the inactivation curve with Eq. 2, and the best fit λ_m^* of S350A mutant was found to be 0.011min^{-1} (Fig. 4E). Calculating replication time with the Hill model, we found that the number of activations predicted by our model satisfied the experimental measurements in the S350A mutant (Fig. 4E). Through our phenomenological model, we could also predict the expectation of X and the minimum HU concentrations required for observable multiple activation phenomena for various mutant strains (Online Supplementary Fig. S11). Irrespective of HU concentration, our findings show that multiple activations might not be observed if the mutation

significantly reduces λ_m. This also explains the absence of Poisson process activations in other autophosphorylation site mutants, such as *rad*53-T354A, as suggested above.

Discussion

The S-phase checkpoint signaling transduction pathway is evolutionarily conserved in eukaryotic cells. In response to DNA replication stress, S-phase checkpoint is activated to repair the stalled DNA replication process. Once DNA replication stress is relieved and the checkpoint is inactivated, S-phase checkpoint might be reactivated by the new DNA stress or persistent signals, resulting in multiple activations. In our previous work, we summarized activation in association with the positive feedback of kinase phosphorylation as a barrier-crossing process in a double-well potential triggered by noise (19). However, the S-phase checkpoint signal transduction pathway is a dynamic process that includes both activation and recovery processes, triggered in response to DNA replication stress signal. It is therefore important to study complex dynamics over the entire time course of S-phase checkpoint.

In general, a signaling network with coupled positive-negative feedback loops may demonstrate oscillatory behaviors, such as those in p53 and NF-κB signaling networks (23, 35). Here, we reported a Poisson activation process of the S-phase checkpoint signal transduction pathway in a single-cell cycle. We studied the dynamics of multiple activations within single cells at different levels of HU and found that stochastic waiting times between consecutive activations are exponentially distributed and independent from each other. This indicates that multiple activation events form a Poisson process. In addition, a key feature of the Poisson process is that the number of events within a given time duration follows a Poisson distribution. In the case of S-phase checkpoint, we found that the level of HU affected both activation rate (λ) and duration of DNA replication (T) in such distribution. Therefore, we used a phenomenological model to show that the number of activations among cell populations at different levels of HU agreed well with a Poisson distribution parametrized by HU, providing strong quantitative evidence for the observed Poisson process. Overall, we provided experimental evidence that the stochastic Poisson process, instead of previously conceived limit cycles, could be emerge from biological pathways that exhibit strong noise effects coupled positive-negative feedback loops. Besides, the DNA damage checkpoint shares similarities with the S-phase (DNA replication) checkpoint, with the same key kinase Rad53. Also, the DNA damage checkpoint can be triggered at various stages of the cell cycle, including the G1/S transition, S-phase, and G2/M boundary (36). Given these similarities, it is plausible that the activation of the DNA damage checkpoint may also follow a Poisson process during cell cycles induced by DNA-damaging drugs, which needs further investigation.

We suggest that the Poisson activation process is mainly determined by two biological factors. First, the limited number of Rad53 molecules leads to stochastic fluctuations in the autophosphorylation chemical reaction. In detail, the positive feedback mechanism of Rad53 autophosphorylation sets a threshold for activation, while the noise-driven over-threshold behavior of Rad53p results in an exponential distribution of waiting times. Second, the efficient recovery process of the S-phase checkpoint returns the cellular state to a level closely resembling its preactivation state, as evidenced by the fact that the waiting times for multiple activations follow the same exponential distribution. Consequently,

the recovery process sets the stage for subsequent activations. Therefore, biochemical reaction noise raised from a limited number of molecules and complete recovery processes are the determining factors of the S-phase checkpoint Poisson activation processes.

The Poisson activation process in the S-phase checkpoint serves potential biological functions. First, these activations are highly stochastic, which stands in contrast to oscillatory dynamics where the intervals between activations fluctuate around fixed values. This stochastic nature of S-phase checkpoint activations leads to variability among cells in a population when exposed to the same external stimulus, where this diversity in response strategies enhances the cell's ability to effectively defend against environmental challenges (37). Second, the independently and identically distributed waiting times of the Poisson activation process mean that cells essentially return to their initial state after each checkpoint activation, which enables yeast cells to promptly respond to subsequent DNA replication stress signals following recovery processes.

For individual cells, the independence of the waiting times between different activations actually rules out the possibility that cell-to-cell variability of activation totally arises from inherent differences among cells (38). Moreover, we investigated the effect of extrinsic noise on the number of activations by assuming that the activation rate λ follows a Gaussian distribution in a cell population, and found that the introduction of extrinsic noise did not noticeably affect the number of cell activations (Fig. 4C and Online Supplementary Fig. S12). Thus, in the context of single-cell cycle activations, we suggest that cell-to-cell variability originates from biochemical reaction noise arising from Rad53 phosphorylation or upstream signaling. At the molecular level, waiting time τ includes both the time of Rad53 phosphorylation and the time of upstream signal accumulation and transduction, which is hard to separate them from τ by our current method. Constructing kinase translocation reporters of Rad53 may be a possible approach to distinguish the time of Rad53 phosphorylation and the time of upstream signal accumulation from τ (39).

In a yeast cell, the number of Rad53 molecules varies from 1,000 to 2,000 (40); thus, the intrinsic noise in Rad53 phosphorylation can determines the waiting time for activation. Given the evolutionary conservation of the S-phase checkpoint, it is likely that the noise characteristics associated with it will persist across different species that have a limited number of Rad53 analogs. However, within mammalian cells, both cell volume and the quantity of each specific protein in a single cell (approximately 10^5/cell) significantly surpass those in budding yeast (2). This means that the effect of noise in mammalian cells will be much smaller than that in yeast cells. In this case, S-phase checkpoint might convert from a Poisson process to a deterministic oscillatory system under high intensity of DNA replication stress. Chk2, the human homolog of Rad53 in the evolutionarily conserved S-phase checkpoint, may demonstrate oscillatory behavior under sufficient DNA replication stress. Similarly, in mammalian cells, p53 is a decisive transcription factor for DNA damage repair, demonstrating conserved oscillatory behaviors across species (23, 41). Overall, in a cell with a large number of Rad53 molecules, such as Rad53-overexpressing strains, we predict that internal noise will not significantly affect the Rad53 phosphorylation process and that all cells may share a similar waiting time. We will explore this possible bifurcation of the S-phase checkpoint pathway in future work.

Our study has some limitations. First, the 5-min resolution in imaging was too low to study the detailed distribution of

activation durations A_1 and A_2 (Online Supplementary Fig. S10), while improving the temporal resolution will reduce the number of observed cells. Also, deficiencies in time accuracy make it difficult to distinguish between two activations that are close in time; thus, some cells exhibited a considerably longer activation duration than others. By refining the structure of microfluidic chip or the imaging method, it may be possible to improve temporal resolution while maintaining the number of cells observed. Second, we estimated Rad53p level by the growth rate of Rnr3. However, since Rad53p upregulates Rnr3 through transcription and translation, the presence of transcription and translation may result in a slight overestimation of the measured waiting time for the first activation. Limited by the Rnr3-based method, it is also hard to directly distinguish Rad53 phosphorylation time and upstream signaling time from τ.

Overall, we identified the Poisson activation process from the S-phase checkpoint pathway in budding yeast, which may provide insights into the complex stochasticity in other signaling transduction pathways or biological processes.

Materials and methods

Yeast strains and cell culture

We used the budding yeast S. *cerevisiae* to investigate the multiple activations of S-phase checkpoint. By fusing GFP to Rnr3, Rnr3-GFP can act as a reporter to identify the activation state of S-phase checkpoint. We called the BY4741 *RNR3-GFP* WT strain as WT in this study. In addition, the *rad53-S350A* mutant, which reduces the autophosphorylation of Rad53p, was used to test the reliability of our model. Both strains in this study come from our previous work (19).

We used two media (YPAD and SC) in this study. One liter of YPAD solid media includes 120 mg adenine, 20 g peptone, 10 g yeast extract, 20 g glucose, and 20 g agar. One liter of SC solid media contains 6.7 g yeast nitrogen base without amino acids (YNB), 2 g dropout mix, 20 g glucose, and 20 g agar. YPAD and SC liquid media can be achieved by removing agar from the recipe above. SC media with HU can be obtained by mixing 1 M HU solution and SC media.

To obtain cells suitable for imaging, we picked a single colony of yeast (WT or mutant) from YPAD plates and cultured it overnight at 30° in YPAD liquid media. Afterward, we extracted the cells by centrifugation and transferred them to SC media for another 2 h. Finally, we adjusted the cell density to OD = 0.8 and injected cells into the microfluidic chip for imaging.

Time-lapse imaging

To facilitate the adjustment of the cell growth environment, we injected the cells into the microfluidic chip for imaging. The microfluidic chip we used comes from past research (42). It contains four channels, and each channel has 40 chambers distributed on both sides of the channel. After cells were injected into the microfluidic chip, we used a syringe pump (Longer, China) to continuously inject HU-free SC media into the chip and observed cell growth status by bright-field (BF) microscopy channel for 2 h. The speed of injection was 66.67 μl/h. To avoid air bubbles from entering the microfluidic chip during imaging, the SC media with HU for injection were configured 4 h in advance of use, along with ensuring that the syringe was free of air bubbles when connected to the chip. After that, we switched the cell growth environment to SC media with HU for formal imaging.

Images were collected in a Nikon Ti-E inverted microscopy (Nikon Co., Japan) with 100× objective and an Evolve 512 EMCCD camera (Photometrics, USA). SOLA Light Engine (Lumencor, USA) provided both white light and fluorescence. NIS Elements AR software (Nikon Co., Japan) was used to select observation points and control the imaging process. We also used a temperature incubator (World Precision Instruments Inc., USA) to provide a stable 30° external environment during imaging.

We used BF and green fluorescence channels to photograph the cells in the microfluidic chip with a 5-min resolution for 8 h. To collect the fluorescence of more cells, we selected 100 observation points. Setting more observation points would have taken more than 5 min to photograph all observation points at once.

Cell segmentation and tracking

We tracked cells from BF images and then extracted cell fluorescence from fluorescent images. We performed cell segmentation on BF images by the U-net-based deep learning framework (43). The training set is derived from manually labeled BF images.

Based on the segmented images, we used custom Matlab code to identify and track cells, as well as extract the fluorescence data. We manually calibrated the traces for each cell and eliminated cells that were tracked incorrectly. We used the average intracellular fluorescence minus the background fluorescence as the fluorescence data of the cells. The effect of image segmentation and cell tracking is shown in Online Supplementary Fig. S13. Our method is stable and able to extract more than 300 cells in one single imaging. We regard the moment of budding as the marker for entering S-phase, and we only collected fluorescence data from the first budding moment to the second budding moment for all cells after HU administration. We have open-sourced the code at Zenodo (https://doi.org/10.5281/zenodo.7898069).

Calculation of FGR and MFGR

The reliability of using the MFGR distribution to distinguish activated cells has been validated by previous work (19). After collecting data from the fluorescent sequencing of single cells, we used a 15-min time-window fitting method to calculate FGR, consisting of four consecutive time points of data ($R = 4$; four time points are t, $t + 5$, $t + 10$ and $t + 15$ min) which were used to perform a linear fit. The slope obtained from the fit is the FGR in time $t + 7.5$. Thus, the FGR starts at 7.5 min and ends at the last time point of cell data minus 7.5 min. We investigated the influence of other R values on our results in Online Supplementary Fig. S8. The activation rates become robust for R$\geq$ 4, and λ_1 and λ_2 are close. Since increasing R can lead to the loss of time point, $R = 4$ or 5 may be the best choice.

The MFGR of a cell at moment t is defined as the maximum value of FGR during time $[0, t]$, i.e. $MFGR(t) \triangleq \max_{0 \leqslant s \leqslant t} FGR(s)$. Given cell-to-cell variability in the activation process, MFGR can well distinguish activated from inactivated cells if we only care whether the cells have been activated or not. The bimodal distribution of MFGR of a cell population demonstrates the binary response pattern of cell activation. By comparing the boundary of MFGR bimodal distribution with the FGR of a single cell, we can determine whether the cell is in an activated state and calculate the time of activation and inactivation. To avoid the influence of fluctuating fluorescence, when the FGR of two consecutive points (t, $t+5$ min) is greater than the boundary, we consider the cell to be activated at moment t. After activation, when two consecutive points (t, $t+5$ min) are smaller than the boundary, we consider the cell to be inactivated at moment t.

The number of activation times X in S-phase

Based on our findings, we proved that the multiple activations of S-phase checkpoint are independent and have the same activation rate λ, i.e. a Poisson process. When we assume that DNA replication time T is not dependent on the number of activations X, the time interval between two activations τ follows an exponential distribution as $P(\tau) = \lambda e^{-\lambda \tau}$. The number of activations X in unit time follows a Poisson distribution, such that the probability that $X = k$ in unit time can be found by $P(X = k) = \frac{\lambda^k}{k!} e^{-\lambda}$, $k = 0, 1, 2, \ldots$.

The stationary increments of activations, or $X(t + s) - X(s)$, $t > s$, are Poisson with mean λt, i.e.

$$P(X(t + s) - X(s) = k) = \frac{(\lambda t)^k}{k!} e^{-\lambda t}, \quad k = 0, 1, 2, \ldots.$$

Expectation $E(X(t + s) - X(s)) = \lambda t$, and variance $Var(X(t + s) - X(s)) = \lambda t$. For the DNA replication process, we set $t = T$ and $s = 0$ in the equation above to calculate the distribution for the number of activations. The distribution of the number of activations $X(\lambda, T)$ during DNA replication time T follows:

$$P(X(\lambda, T) = k) = \frac{(\lambda T)^k}{k!} e^{-\lambda T}, \quad k = 0, 1, 2, \ldots.$$

The DNA replication time T and activation rate λ are dependent on the concentration of HU in our system.

Fitting the relations between HU concentration and activation rate λ or total DNA replication time T

In our study, we adopted the least squares method to fit the relationship between the activation rate λ and HU concentration by Eq. 2. The standard deviation of each parameter was estimated as the arithmetic square root of the diagonal elements of the covariance matrix of the fitted results. Afterward, based on the data of X, we fitted the relationship between DNA replication time T and HU concentration by Eq. 1 with the same method. The mean and SD of the parameters obtained by fitting are listed in Table 1.

Statistical analysis of activation rate estimation and independence test with truncated time

Assume that σ_1 and σ_2 are two independently and exponentially distributed random variables with rate parameter λ. Within the observation period $[0, T]$, define the two observed activation times such that

$$\tau_1 = \begin{cases} \sigma_1, & \sigma_1 \leq T \\ +\infty, & \sigma_1 > T \end{cases}$$

and

$$\tau_2 = \begin{cases} \sigma_2, & \sigma_1 + \sigma_2 \leq T \\ +\infty, & \sigma_1 + \sigma_2 > T. \end{cases}$$

Then for fixed $t < T$ we have

$$P(\tau_1 > t) = \exp(-\lambda t),$$

which proves that the rate of first activation can be estimated through the regression between $-\ln P(\tau_1 > t)$ and t in the linear region of a graph. In particular, the consistency and convergence rate of such statistical estimator has been studied in Ref. (19).

For the second activation, the inactivation curve for regression was based on the conditional probability which assumes that the first activation has been observed within $[0, T]$, i.e.

$$\begin{aligned} P(\tau_2 > t \mid \tau_1 < T) &= 1 - P(\tau_2 \leq t \mid \tau_1 < T) \\ &= 1 - P(\sigma_2 \leq t, \sigma_1 + \sigma_2 \leq T \mid \sigma_1 < T) \\ &= 1 - \frac{P(\sigma_2 \leq t, \sigma_1 < T, \sigma_1 + \sigma_2 \leq T)}{1 - \exp(-\lambda T)} \\ &= \frac{\exp(\lambda(T - t)) + \lambda t - 1}{\exp(\lambda T) - 1}. \end{aligned}$$

To justify regression using the inactivation curve, we observe that

$$-\ln P(\tau_2 > t \mid \tau_1 < T) = \lambda t - \frac{\lambda^2 t^2}{2(\exp(\lambda T) - 1)} + O(\lambda^3 t^3).$$

Therefore, the estimation of λ using the slope of the inactivation curve could still be accurate as long as the ground-truth λ is small and the time points used for regression are within the shorter time interval compared to the overall DNA replication time T, which is the case for the data we analyzed.

To analyze the independence test, we observe that for $t_1 + t_2 < T$,

$$\begin{aligned} &P(\tau_1 \in [t_1, t_1 + \Delta t_1], \tau_2 \in [t_2, t_2 + \Delta t_2] \mid \tau_1 < T) \\ &= \frac{P(\tau_1 \in [t_1, t_1 + \Delta t_1], \tau_2 \in [t_2, t_2 + \Delta t_2])}{P(\tau_1 < T)} \\ &= \frac{P(\sigma_1 \in [t_1, t_1 + \Delta t_1], \sigma_2 \in [t_2, t_2 + \Delta t_2])}{1 - \exp(-\lambda T)} \\ &\approx \frac{\lambda^2 \exp(-\lambda(t_1 + t_2))}{1 - \exp(-\lambda T)} \Delta t_1 \Delta t_2 \end{aligned}$$

and

$$\begin{aligned} &P(\tau_1 \in [t_1, t_1 + \Delta t_1] \mid \tau_1 < T) P(\tau_2 \in [t_2, t_2 + \Delta t_2] \mid \tau_1 < T) \\ &\approx \frac{\lambda^2 \exp(\lambda(T - t_1))(\exp(\lambda(T - t_2)) - 1)}{(\exp(\lambda T) - 1)^2} \Delta t_1 \Delta t_2. \end{aligned}$$

Therefore, we have

$$\begin{aligned} &\mid P(\tau_1 \in [t_1, t_1 + \Delta t_1], \tau_2 \in [t_2, t_2 + \Delta t_2] \mid \tau_1 < T) \\ &\quad - P(\tau_1 \in [t_1, t_1 + \Delta t_1] \mid \tau_1 < T) P(\tau_2 \in [t_2, t_2 + \Delta t_2] \mid \tau_1 < T) \mid \\ &= \frac{\exp(\lambda T) \lambda^3 t_2}{(\exp(\lambda T) - 1)^2} \Delta t_1 \Delta t_2 + O(\lambda^4), \end{aligned}$$

suggesting that validity of the independence test using probability density still holds with truncated time, as long as λ is small and T is larger than the time points used for test.

Similarly, for the cumulative distribution function, we also have

$$\begin{aligned} &\mid P(\tau_1 < t_1, \tau_2 < t_2 \mid \tau_1 < T) \\ &\quad - P(\tau_1 < t_1 \mid \tau_1 < T) P(\tau_2 < t_2 \mid \tau_1 < T) \mid \\ &= \frac{\exp(\lambda T) \lambda^3 t_1 t_2^2}{2(\exp(\lambda T) - 1)^2} + O(\lambda^4), \end{aligned}$$

indicating that independence could also be observed from inactivation curve probabilities (Online Supplementary Fig. S9).

Acknowledgments

Supplementary Material

Supplementary material is available at *PNAS Nexus* online.

Funding

Author Contributions

F.L. designed the research, X.G. performed the experiments and mathematical modeling, P.Z contributed to statistical and theoretical analysis, X.G. and P.Z wrote the manuscript.

Data Availability

All study data are included in the article and/or SI Appendix. The analysis code can be found at Zenodo (https://doi.org/10.5281/zenodo.7898069).

References

1   Balázsi G, Van Oudenaarden A, Collins JJ. 2011. Cellular decision making and biological noise: from microbes to mammals. *Cell*. 144(6):910–925.

2   Alon U. 2019. *An introduction to systems biology: design principles of biological circuits*. 2nd ed. Boca Raton (FL): Chapman and Hall/CRC.

3   Martinez-Corral R, Raimundez E, Lin Y, Elowitz MB, Garcia-Ojalvo J. 2018. Self-amplifying pulsatile protein dynamics without positive feedback. *Cell Syst*. 7(4):453–462.e1.

4   Ahrends R, *et al.* 2014. Controlling low rates of cell differentiation through noise and ultrahigh feedback. *Science*. 344(6190):1384–1389.

5   Li Y, *et al.* 2020. Noise-driven cellular heterogeneity in circadian periodicity. *Proc Natl Acad Sci USA*. 117(19):10350–10356.

6   Desai RV, *et al.* 2021. A DNA repair pathway can regulate transcriptional noise to promote cell fate transitions. *Science*. 373(6557):eabc6506.

7   Eling N, Morgan MD, Marioni JC. 2019. Challenges in measuring and understanding biological noise. *Nat Rev Genet*. 20(9):536–548.

8   Heltberg M, Kellogg RA, Krishna S, Tay S, Jensen MH. 2016. Noise induces hopping between NF-κB entrainment modes. *Cell Syst*. 3(6):532–539.e3.

9   Yao J, Pilko A, Wollman R. 2016. Distinct cellular states determine calcium signaling response. *Mol Syst Biol*. 12(12):894.

10 Tanaka K, Augustine GJ. 2008. A positive feedback signal transduction loop determines timing of cerebellar long-term depression. *Neuron*. 59(4):608–620.

11 Ferrell JE Jr., Ha SH. 2014. Ultrasensitivity part II: multisite phosphorylation, stoichiometric inhibitors, and positive feedback. *Trends Biochem Sci*. 39(11):556–569.

12 Cheng QJ, *et al.* 2021. NF-κB dynamics determine the stimulus specificity of epigenomic reprogramming in macrophages. *Science*. 372(6548):1349–1353.

13 Louis M, Becskei A. 2002. Binary and graded responses in gene networks. *Sci STKE*. 2002(143):pe33–pe33.

14 Zhang Q, *et al.* 2017. NF-κB dynamics discriminate between TNF doses in single cells. *Cell Syst*. 5(6):638–645.

15 Pelkmans L. 2012. Using cell-to-cell variability–a new era in molecular biology. *Science*. 336(6080):425–426.

16 Padovan-Merhar O, *et al.* 2015. Single mammalian cells compensate for differences in cellular volume and DNA copy number through independent global transcriptional mechanisms. *Mol Cell*. 58(2):339–352.

17 Liu Y, *et al.* 2021. The intra-S phase checkpoint directly regulates replication elongation to preserve the integrity of stalled replisomes. *Proc Natl Acad Sci USA*. 118(24):e2019183118.

18 Segurado M, Tercero JA. 2009. The s-phase checkpoint: targeting the replication fork. *Biol Cell*. 101(11):617–627.

19 Zhou P, *et al.* 2021. Stochasticity triggers activation of the S-phase checkpoint pathway in budding yeast. *Phys Rev X*. 11:011004.

20 Clémenson C, Marsolier-Kergoat M-C. 2009. DNA damage checkpoint inactivation: adaptation and recovery. *DNA Repair (Amst)*. 8(9):1101–1109.

21 Chen SH, Smolka MB, Zhou H. 2007. Mechanism of Dun1 activation by Rad53 phosphorylation in *Saccharomyces cerevisiae*. *J Biol Chem*. 282(2):986–995.

22 Ashall L, *et al.* 2009. Pulsatile stimulation determines timing and specificity of NF-κB-dependent transcription. *Science*. 324(5924):242–246.

23 Hafner A, Bulyk ML, Jambhekar A, Lahav G. 2019. The multiple mechanisms that regulate p53 activity and cell fate. *Nat Rev Mol Cell Biol*. 20(4):199–210.

24 Zeman MK, Cimprich KA. 2013. Causes and consequences of replication stress. *Nat Cell Biol*. 16(1):2–9.

25 Koç A, Wheeler LJ, Mathews CK, Merrill GF. 2004. Hydroxyurea arrests DNA replication by a mechanism that preserves basal dNTP pools. *J Biol Chem*. 279(1):223–230.

26 Xie M, *et al.* 2014. Bcl2 induces DNA replication stress by inhibiting ribonucleotide reductase. *Cancer Res*. 74(1):212–223.

27 Chen G, *et al.* 2019. Acetylation regulates ribonucleotide reductase activity and cancer cell growth. *Nat Commun*. 10(1):1–16.

28 Bacal J, *et al.* 2018. Mrc1 and Rad9 cooperate to regulate initiation and elongation of DNA replication in response to DNA damage. *EMBO J*. 37(21):e99319.

29 Forey R, *et al.* 2020. Mec1 is activated at the onset of normal S phase by low-dNTP pools impeding DNA replication. *Mol Cell*. 78(3):396–410.e4.

30 Alvino GM, *et al.* 2007. Replication in hydroxyurea: it's a matter of time. *Mol Cell Biol*. 27(18):6396–6406.

31 Sheu Y-J, Stillman B. 2010. The Dbf4-Cdc7 kinase promotes S phase by alleviating an inhibitory activity in Mcm4. *Nature*. 463(7277):113–117.

32 Vincent Tang H-M, Siu K-L, Wong C-M, Jin D-Y. 2009. Loss of yeast peroxiredoxin Tsa1p induces genome instability through activation of the DNA damage checkpoint and elevation of dNTP levels. *PLoS Genet*. 5(10):e1000697.

33 Van der Maaten L, Hinton G. 2008. Visualizing data using t-SNE. *J Mach Learn Res*. 9(11):2579–2605.

34 Sekedat MD, *et al.* 2010. GINS motion reveals replication fork progression is remarkably uniform throughout the yeast genome. *Mol Syst Biol*. 6(1):353.

35 Qiao L, Zhang Z-B, Zhao W, Wei P, Zhang L. 2022. Network design principle for robust oscillatory behaviors with respect to biological noise. *eLife*. 11:e76188.

36 Pellicioli A, *et al.* 1999. Activation of Rad53 kinase in response to dna damage and its effect in modulating phosphorylation

of the lagging strand DNA polymerase. *EMBO J.* 18(22): 6561–6572.

37 Snijder B, Pelkmans L. 2011. Origins of regulated cell-to-cell variability. *Nat Rev Mol Cell Biol.* 12(2):119–125.

38 Charlebois DA, Hauser K, Marshall S, Balázsi G. 2018. Multiscale effects of heating and cooling on genes and gene networks. *Proc Natl Acad Sci USA.* 115(45):E10797–E10806.

39 Regot S, Hughey JJ, Bajar BT, Carrasco S, Covert MW. 2014. High-sensitivity measurements of multiple kinase activities in live single cells. *Cell.* 157(7):1724–1734.

40 Ghaemmaghami S, *et al.* 2003. Global analysis of protein expression in yeast. *Nature.* 425(6959):737–41.

41 Stewart-Ornstein J, Jacky Cheng HW, Lahav G. 2017. Conservation and divergence of p53 oscillation dynamics across species. *Cell Syst.* 5(4):410–417.

42 Luo C, *et al.* 2009. High-throughput microfluidic system for monitoring diffusion-based monolayer yeast cell culture over long time periods. *Biomed Microdevices.* 11(5):981.

43 Ronneberger O, Fischer P, Brox T. 2015. U-net: convolutional networks for biomedical image segmentation. In: Medical Image Computing and Computer-Assisted Intervention—MICCAI 2015: 18th International Conference, Munich, Germany, October 5–9, 2015, Proceedings, Part III 18. Springer International Publishing. p. 234–241.